Case Studies in Thermal Engineering 49 (2023) 103230

Contents lists available at ScienceDirect

Case Studies in Thermal Engineering

journal homepage: www.elsevier.com/locate/csite

Mathematical model of ciliary flow and entropy for carreau nanofluid with electroosmosis and radiations in porous medium: A numerical work

Wafa F. Alfwzan [a], F.M. Allehiany [b], Arshad Riaz [c,*], Sheraz Sikandar [c], Ghaliah Alhamzi [d]

[a] Department of Mathematical Sciences, College of Science, Princess Nourah bint Abdulrahman University, P.O. Box 84428, Riyadh, 11671, Saudi Arabia
[b] Department of Mathematical Sciences, College of Applied Sciences, Umm Al-Qura University, Saudi Arabia
[c] Department of Mathematics, Division of Science and Technology, University of Education, Lahore, 54770, Pakistan
[d] Department of Mathematics and Statistics, College of Science, Imam Mohammad Ibn Saud Islamic University (IMSIU), Riyadh, Saudi Arabia

ARTICLE INFO

Handling Editor: Huihe Qiu

Keywords:
Cilia flow
Ternary-hyrbrid nanofluid
Carreua fluid
Electroosmosis and Entropy generation
Thermal radiations
Shooting method

ABSTRACT

Functionalizing the nanoparticles like titanium oxide (TiO_2), silica (SiO_2), and aluminum oxide (AI_2O_3) with therapeutic agents like anticancer drugs, antibiotics, or gene therapy agents allow targeted delivery and controlled release. We investigate how thermal radiation in Carreau constitutive model base liquid (blood) affects the flow of a ternary-hybrid nanofluid made of the said particles. Connecting the conduit to battery terminals outside accounts for entropy and electroosmosis. After translating the observation model into a wave frame, lubrication theory's physical limits are used to better explain the wave phenomena. The study uses Mathematica NDSolve to simulate boundary value issues using shooting. The Carreau fluid has a 17–18% higher heat transfer rate than the Williamson fluid, according to the literature. Elastic electroosmotic pumping, cilia motion, and magnetic fields improve fluid transport. Ternary hybrid nanofluids improve transport mechanisms and thermal conductivity. Elastic electroosmotic pumping and cilia motion produce the least entropy and increase thermodynamic efficiency.

1. Introduction

Ciliary fluxes aid biomedical, microfluidic, and industrial processes. Cilia transmit mucus and other particles via the respiratory and reproductive channels. Cilia-inspired microfluidics pumps and mixers are efficient. Cilia-inspired surfaces improve fluid flow and thermal transmission in microchannels. Cilia flows are researched in oil extraction and filtration. Cilia flow and its uses are extensively studied. Sleigh [1] discussed cilia structure and metachronal wave patterns in 1962. Using sublayer and envelope models, cilia pulsing causes fluid transfer. Any location outside or within the cilia layer can have its average or immediate velocity determined by applying the sublayer concept. However, only distant cilia work. Blake [2,3] first studied the infinite plan wall sublayer model, then added two parallel walls. The envelope notion states that a densely packed envelope of cilia tip profiles determines a fluid's velocity field's outermost layer. This paradigm represents several biological processes. Shack and Lardner [4] utilized a cilia-model technique to study fluid movement in the male reproductive system's ductus efferentes based on a metachronal wave's symplectic pattern. Akbar and

* Corresponding author.
E-mail address: arshad-riaz@ue.edu.pk (A. Riaz).

https://doi.org/10.1016/j.csite.2023.103230
Received 7 May 2023; Received in revised form 16 June 2023; Accepted 24 June 2023
Available online 26 June 2023
2214-157X/

Akhtar [5] have acquired analytical solutions for cilia-based flow for the non-linear fluid model in a channel. More studies on the topic can be cited in [6–10].

The improved thermal and physical properties of ternary hybrid nanofluids over conventional fluids are driving their rising popularity. These fluids contain three types of nanoparticles, all of which contribute to the fluids' overall effectiveness. Ternary hybrid nanofluids have numerous industrial and medical applications. Ternary hybrid nanofluids may one day improve the efficiency of heat exchangers, refrigerators, and microelectronics coolers at the workplace. These devices have a wide range of applications, including bio-physical pumps, heating pumps, drug transporting pumps, emollient, mini-mixers, and cooling. In a landmark work, Choi [11] developed the concept of nanofluids. Researchers have recently investigated the notion of ternary fluids, with tri-metallic nanoparticles were disseminated in a pure liquid. Ternary nanofluids have been experimentally explored, and the findings [12,13] describe their extraordinary properties and implications. There have been few theoretical efforts to examine the beneficial and sensitive role of such nano-fluids in increasing thermal transmission. In this connection, Manjunatha et al. [14] suggested a mathematical tri-hybrid nanoliquid model to explain increased thermal exchange properties. Elnaqeeb et al. [15] investigated the study of porosity on ternary nanosubstances in water. Munawar and Saleem [16] recently performed a heat exchange measures of Williamson nanofluid mixed with three various particles and found that, in comparison to hybrid and mono nanofluids, radiated ternary fluid had superior heat transfer capabilities. Additional research on nanofluids is discussed in references [17–20].

Electric fields cause electroosmotic motion in liquids. The electric ions at the dual interface maintains net charge density and drives this flow. Electroosmotic fluid pumps, test procedure for DNA, biological drug delivery pumps, cooling strips, lab-on-a-chip machine, microfabrication are used in micro and nanofluidic devices. Burgreen and Nakache [21] pioneered this approach in 1964. Abo-Elkhair et al. [22] evaluated an electro-hdrodynamic and surface slip conditions in wavy motion and found that strong electroosmotic parameters impede fluid velocity near microchannel walls. Micro-fluidics and micropumps can benefit from Chaube et al.'s [23] research on electric fields and non-Newtonian liquids. Ramesh et al. [24] theoretically analyzed how an axially applied electric field affects Jeffrey fluid peristaltic motion. Javayel et al. found that electroosmotic parameters increase pump wall skin friction [25]. Hang et al. explored electroosmosis-driven stream in a microchannel with an extended top border [26]. Recent research on microchannel peristaltic flow is available in Refs. [27–29].

The Carreau fluid is recognized as a non-Newtonian model liquid because its viscosity fluctuates with shear rate. This fluid has been used to simulate blood circulation in the human body. It can be used to forecast how blood will behave in a variety of conditions because to its non-Newtonian features. It is used in a variety of industrial operations, ranging from polymer processing to chemical manufacturing. Because of its non-Newtonian qualities, it can be employed to improve flow control and quality. Mahdy et al. [30] ran numerical simulations of the Carreau model's heat exchange stream in a thermal cylinder with changing conductivity. Alloui and Vasseur [31] investigated and reviewed several models used to analyze the rheological behavior of non-Newtonian fluids, including Carreau fluids. Raju et al. [32] investigated the forced convective heat transfer of a Carreau fluid in a square ductile shape using computational methods. Increased Reynolds numbers and the power-law index minimum are discovered to increase heat transfer rate. Lim et al. [33] studied the natural convection of a Carreau liquid in a vertical cylinder analytically.

Magnetohydrodynamic (MHD) fluxes have been employed by numerous researchers to gain insight into cilia motility, which has significant implications across many fields of biology and medicine. Cilia are tiny, hair-like structures that serve crucial roles in fluid transport, sensing, and motion and are found in a wide variety of organisms, including humans. A conducting fluid's velocity changes as a result of the Lorentz force applied by a magnetic field. The use of MHD flows allows researchers to examine how external magnetic fields affect ciliary beating and the fluid movement caused by the cilia. The effects of a fluctuating magnetic field on the pumping of blood and the transfer of heat were studied by Stud et al. [34]. Hydromagnetic physiological flow was further studied by Maqbool et al. [35], who focused on Jeffrey fluid flow caused by cilia beating. The velocity at the boundary wall increases with increasing magnetic Hartmann number, but the velocity in the core region decreases, as observed by Hayat et al. [36]. In the presence of a magnetic field, Ramesh et al. [37] investigated pair stress fluid flow prompted by pumping cilia. Other researchers [38–41] have looked into how an external magnetic field affects various bodily fluids.

Transport through porous media is essential to many mechanical, biological, and engineering processes [42,43]. Several models, including the Darcy, Darcy-Forchecimer, and Brinkman-extended Darcy, have been proposed in the literature for the investigation of porous media [44]. The Darcy rule was used by Akbar et al. [45] to describe the slow currents within the ciliated tube. Using a ciliated channel, Manzoor et al. [46] looked into the efficient qualities of the viscoelastic model (Jeffrey fluid). The Adomian decomposition method (ADM), which accounts for MHD alongside porous media and convective heat transport, was used to arrive at the corresponding mathematical solutions. In a porous medium containing Jeffrey fluid, Javid et al. [47] used the BVP4C approach to find a numerical solution for a diverging ciliated channel. Using a cilia-oriented cylindrical tube, Aich et al. [48] studied the effect of hybrid nanofluids on porosity. The study of various heat- and mass-transport applications in biology and medicine, using engineering's foundational concepts, has led to significant advances in our understanding of the thermal and mechanical characteristics of human tissue, which ultimately control the biological process. Bioheat-transfer phenomena have gained significant attention in the last twenty years for their potential therapeutic and diagnostic uses. The advancement of mathematical models supported by state-of-the-art computational tools has greatly facilitated the study of many flavors of the bioheat-transfer process [49–53]. Using the Darcy-Forchheimer theory for porous medium with heat transfer, Usman et al. [54] thought about the Williamson fluid passing via a ciliated channel.

Hyperthermia and medical imaging are both helped by the Carreau nanofluid. Cancer patients can receive tailor-made heat treatments thanks to the use of magnetic nanofluid. Since the Carreau nanofluid has such remarkable rheology, it enhances imaging contrast and resolution. Hybrid nanofluids and improved flow control methods may increase the effectiveness of such tools by facilitating more effective fluid transfer. However, it is challenging to grasp the underlying mechanics because of the intricate

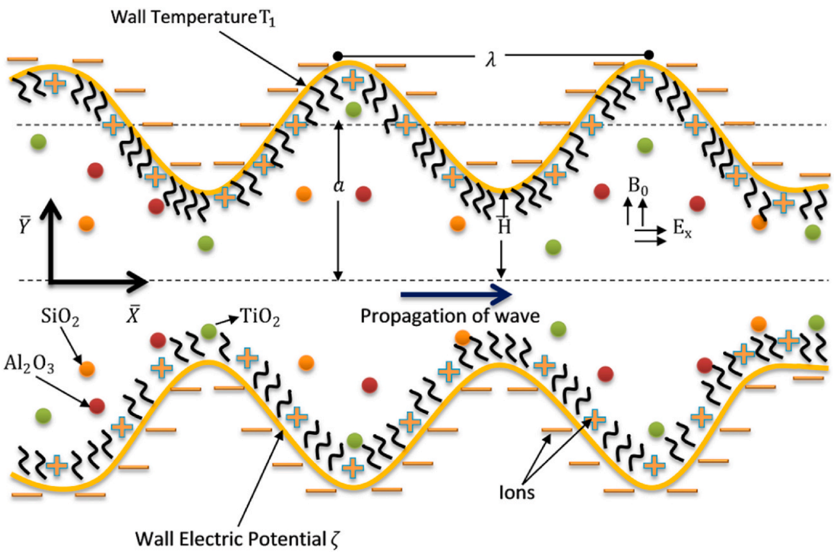

Fig. 1. Schematic representation of cilia-controlled electro-osmotic motion of ternary nanofluid.

connections between fluid flow, magnetic fields, and cilia motility. Therefore, the purpose of this research is to give a comprehensive assessment of the efficacy of several fluid transport strategies for investigating the propagation of ternary-hybrid nanofluids in Carreau model fluids. New, more effective technologies should result from research into the underlying mechanics of these intricate systems. Numerical simulations will be run utilizing computational fluid dynamics (CFD) software like Mathematica and MatLab to reach this goal. The impact of an applied magnetic field on a simplified model of cilia motility in a microchannel is to be investigated. Magnetic field orientation and strength, cilia length and flexibility, and the Reynolds and Hartmann numbers will all be put to the test in the simulations. The effects of MHD flows on ciliary beating patterns, fluid transport, and entropy formation will be studied using the simulation results.

2. Mathematical modeling

Let us consider a 2-dimensional motion of mixed convective pumping of a non-linear model of nanofluid across a flexible channel under the effects of electromagnetohydrodynamics (EMHD) and porous medium. The fluid consists of a mixture of electrically conducting base liquid (blood) and tri-hybrid nanofluid containing solid types of nanoparticles of silica (SiO_2), titanium oxide (TiO_2) and aluminum oxide (AI_2O_3). The base fluid, blood, reveals shear-thinning property that can be modeled using the Carreau model. Moreover, a constant magnetic field $\boldsymbol{B} = (0, B_0)$ is inserted in the transverse line of the flow. The flow geometry and coordinate system are illustrated in Fig. 1, with a Cartesian coordinate system set up so that the horizontal X-axis represents the wave propagation axis, and the orthogonal Y-axis is perpendicular to the X-axis.

Function determines the underlying structure of embedded cilia [1–5]:

$$\overline{H}(\overline{X}, t) = a + a\varepsilon \Big/ \sec\left(\frac{2\pi}{\lambda}(\overline{X} - ct)\right), \tag{1}$$

Sleigh [37] did an experimental study that found that cilia movement is characterized by elliptical movements of the cilia tips and the horizontal orientation of the cilia heads, and his findings can be summarized as follows:

$$\overline{G}(\overline{X}, t) = X_0 + \alpha a\varepsilon \Big/ \csc\left(\frac{2\pi}{\lambda}(\overline{X} - ct)\right), \tag{2}$$

Here, a stands for the channel's average width, for the length of the cilia, for the eccentricity of the elliptical track along which the cilia move, for the wavelength, t for the time period, and X_0 for the initial position of the particle. The tangential and transverse components of ciliary velocity can be determined with the help of Equations (1) and (2).

$$\overline{U_0} = \left(\frac{\partial \overline{G}}{\partial t}\right)_{X_0} = \frac{-\left(\frac{2\pi}{\lambda}\right)a\varepsilon\alpha c\cos\left(\frac{2\pi}{\lambda}(\overline{X} - ct)\right)}{1 - \left(\frac{2\pi}{\lambda}\right)a\varepsilon\alpha\cos\left(\frac{2\pi}{\lambda}(\overline{X} - ct)\right)}, \tag{3}$$

$$\overline{V_0} = \left(\frac{\partial \overline{H}}{\partial t}\right)_{X_0} = \frac{\frac{2\pi}{\lambda}a\varepsilon c\sin\left(\frac{2\pi}{\lambda}(\overline{X} - ct)\right)}{1 - \frac{2\pi}{\lambda}a\alpha\varepsilon\cos\left(\frac{2\pi}{\lambda}(\overline{X} - ct)\right)}. \tag{4}$$

The Carreau ternary nanofluid is associated with an extra stress tensor, which is mathematically represented as [30–36]:

Table 1
Thermophysical characteristics of the ternary-hybrid nanofluid [12–15].

Physical quantities	Base fluid (**Blood**)	Nanoparticles		
		T_iO_2	**SiO_2**	**AI_2O_3**
σ $(1/\Omega m)$	0.8	2.4 x 10^6	3.5 x 10^6	36.9 x 10^6
ρ (kg/m^3)	1063	4250	2200	3970
C_p (J /Kkg)	3594	686.2	754	765
k (W /mK)	0.492	8.9538	1.4013	40
β_t (1 /K) x 10^{-6}	0.18	0.9	4.27	8

$$\overline{S} = \mu_{thnf}\left(1 + (\Gamma\overline{\dot{\gamma}})^2\right)^{\frac{n-1}{2}} A_1. \tag{5}$$

Using Equation (5), it is possible to determine the parts of the stress matrix, which can be expressed as follows:

$$\overline{S}_{XX} = 2\mu_{thnf}\left(1 + (\Gamma\overline{\dot{\gamma}})^2\right)^{\frac{n-1}{2}} \frac{\partial \overline{U}}{\partial \overline{X}}, \tag{6}$$

$$\overline{S}_{XY} = \mu_{thnf}\left(1 + (\Gamma\overline{\dot{\gamma}})^2\right)^{\frac{n-1}{2}} \left(\frac{\partial \overline{U}}{\partial \overline{Y}} + \frac{\partial \overline{V}}{\partial \overline{X}}\right), \tag{7}$$

$$\overline{S}_{YY} = 2\mu_{thnf}\left(1 + (\Gamma\overline{\dot{\gamma}})^2\right)^{\frac{n-1}{2}} \frac{\partial \overline{V}}{\partial \overline{Y}}, \tag{8}$$

The problem is simulated by incorporating physical laws such as continuity, momentum, and the heat equation, as well as the previously mentioned assumptions. The following governing equations are in the fixed frame:

$$\frac{\partial \overline{U}}{\partial \overline{Y}} + \frac{\partial \overline{V}}{\partial \overline{X}} = 0, \tag{9}$$

$$\rho_{thnf}\left(\frac{\partial \overline{U}}{\partial t} + \overline{U}\frac{\partial \overline{U}}{\partial \overline{X}} + \overline{V}\frac{\partial \overline{U}}{\partial \overline{Y}}\right) = -\frac{\partial \overline{P}}{\partial \overline{X}} + \frac{\partial \overline{S}_{XX}}{\partial \overline{X}} + \frac{\partial \overline{S}_{XY}}{\partial \overline{Y}} - \sigma_{thnf} B_0{}^2\overline{U} + \rho_e E_X + g(\rho\beta_t)_{thnf}(\overline{T} - \overline{T}_0) - \frac{\mu_{thnf}}{k^*}\overline{U}, \tag{10}$$

$$\rho_{thnf}\left(\frac{\partial \overline{V}}{\partial t} + \overline{U}\frac{\partial \overline{V}}{\partial \overline{X}} + \overline{V}\frac{\partial \overline{V}}{\partial \overline{Y}}\right) = -\frac{\partial \overline{P}}{\partial \overline{Y}} + \frac{\partial \overline{S}_{XX}}{\partial \overline{X}} + \frac{\partial \overline{S}_{XY}}{\partial \overline{Y}}, \tag{11}$$

$$(\rho C_P)_{thnf}\left(\frac{\partial \overline{T}}{\partial t} + \overline{U}\frac{\partial \overline{T}}{\partial \overline{X}} + \overline{V}\frac{\partial \overline{T}}{\partial \overline{Y}}\right) = k_{thnf}\left(\frac{\partial^2 \overline{T}}{\partial \overline{X}^2} + \frac{\partial^2 \overline{T}}{\partial \overline{Y}^2}\right) + \overline{S}_{XX}\frac{\partial \overline{U}}{\partial \overline{X}} + \overline{S}_{XY}\left(\frac{\partial \overline{U}}{\partial \overline{Y}} + \frac{\partial \overline{V}}{\partial \overline{X}}\right) + \overline{S}_{YY}\frac{\partial \overline{V}}{\partial \overline{Y}} - \left(\frac{\partial \overline{q}_r}{\partial \overline{X}} + \frac{\partial \overline{q}_r}{\partial \overline{Y}}\right) + \sigma_{thnf}\left(E_X{}^2 + B_0{}^2\overline{U}^2\right). \tag{12}$$

Based on the presumptions presented here, the flow is subject to certain boundary conditions.

$$\overline{U} = U_0, \overline{T} = T_1 \ at \ \overline{Y} = \overline{H}, \frac{\partial \overline{U}}{\partial \overline{Y}} = 0, \frac{\partial \overline{T}}{\partial \overline{Y}} = 0 \ \ at \ \overline{Y} = 0, \tag{13}$$

The variables used in the equations are as follows: fluid pressure is denoted by $\overline{P}$, fluid temperature by $\overline{T}$ and the components of velocity along the $\overline{X}$ and $\overline{Y}$-axis are denoted by $\overline{U}$ and $\overline{V}$, respectively. The radiative heat flow rate along the X-axis is considered diminishing in contrast to that along the Y-axis. The Rosseland assumption is utilized to express this heat rate q_r as [38]:

$$\overline{q}_r = \frac{-16\sigma^*(\Delta T)^3}{3K^*}\frac{\partial \overline{T}}{\partial \overline{Y}}. \tag{14}$$

The electric-potential function $\overline{\varphi}$ can be defined using the Poisson equation, as presented in Refs. [23–28]:

$$\frac{\partial^2 \overline{\varphi}}{\partial \overline{X}^2} + \frac{\partial^2 \overline{\varphi}}{\partial \overline{Y}^2} = -\frac{\rho_e}{\varepsilon\varepsilon_0}, \tag{15}$$

where

$$\rho_e = -2n_0 ze \sinh\left(\frac{ze\overline{\varphi}}{k_b T_{ave}}\right). \tag{16}$$

Additionally, since the zeta potential at the wall ($\leq 25\,mV$) is negligible, the Debyeh-Hückel approximation is applied, yielding:

$$\sinh\left(\frac{ze\overline{\varphi}}{k_b T_{ave}}\right) \cong \frac{ze\overline{\varphi}}{k_b T_{ave}}. \tag{17}$$

Imposing Eqs. (16) and (17), Eq. (15) becomes

$$\frac{\partial^2 \overline{\varphi}}{\partial \overline{X}^2} + \frac{\partial^2 \overline{\varphi}}{\partial \overline{Y}^2} = \frac{2n_0 z^2 e^2}{k_b T_{ave} \varepsilon \varepsilon_0} \overline{\varphi}. \tag{18}$$

The ternary-hybrid nanofluid is thought to be well-mixed nanoparticles of TiO_2, SiO_2, and $AI_2\,O_3$ in a base fluid (blood). Table 1 lists the thermophysical characteristics of blood and nanoparticles. Several correlations [12–15] characterize the thermophysical characteristics of trihybrid nanofluids.

$$\rho_{thnf} = \left(1-\varphi^T\right)\left[\left(1-\varphi^S\right)\left(\left(1-\varphi^A\right)\rho_f + \varphi^A \rho_A\right) + \varphi^S \rho_S\right] + \varphi^T \rho_T, \tag{19}$$

$$(\rho\beta_t)_{thnf} = \left(1-\varphi^T-\varphi^S-\varphi^A\right)(\rho\beta_t)_f + \varphi^T(\rho\beta_t)_T + \varphi^S(\rho\beta_t)_S + \varphi^A(\rho\beta_t)_{A,} \tag{20}$$

$$(\rho C_P)_{thnf} = \left(1-\varphi^T-\varphi^S-\varphi^A\right)(\rho C_P)_f + \varphi^T(\rho C_P)_T + \varphi^S(\rho C_P)_S + \varphi^A(\rho C_P)_{A,} \tag{21}$$

$$\frac{\sigma_{thnf}}{\sigma_f} = \frac{(1+2\varphi^T)\sigma_T + (1-2\varphi^T)\sigma_{hnf}}{(1-\varphi^T)\sigma_T + (1+\varphi^T)\sigma_{hnf}}, \tag{22}$$

$$\frac{\sigma_{hnf}}{\sigma_f} = \frac{(1+2\varphi^S)\sigma_S + (1-2\varphi^S)\sigma_{nf}}{(1-\varphi^S)\sigma_S + (1+\varphi^S)\sigma_{nf}}, \frac{\sigma_{nf}}{\sigma_f} = \frac{(1+2\varphi^A)\sigma_A + (1-2\varphi^A)\sigma_f}{(1-\varphi^A)\sigma_A + (1+\varphi^A)\sigma_f}, \tag{23}$$

$$\frac{k_{thnf}}{k_{hnf}} = \frac{k_T + 2k_{hnf} - 2\varphi^T\left(k_{hnf} - k_T\right)}{k_T + 2k_{hnf} + 2\varphi^T\left(k_{hnf} - k_T\right)}, \tag{24}$$

$$\frac{k_{hnf}}{k_{nf}} = \frac{k_S + 2k_{nf} - 2\varphi^S\left(k_{nf} - k_T\right)}{k_S + 2k_{nf} + \varphi^S\left(k_{nf} - k_S\right)}, \tag{25}$$

$$\frac{k_{nf}}{k_f} = \frac{k_A + 2k_f - 2\varphi^A\left(k_f - k_A\right)}{k_A + 2k_f + \varphi^A\left(k_f - k_A\right)}, \tag{26}$$

$$\frac{\mu_{thnf}}{\mu_f} = \left(\left(1-\varphi^T\right)\left(1-\varphi^S\right)\left(1-\varphi^A\right)\right)^{-5/2}, \tag{27}$$

The volume fraction of considered nanoparticles is represented by the symbol φ, with alphabetical subscripts and superscripts *T, S* and *A* identifying solid nanoparticles of titanium oxide, silica, and aluminum oxide, orderly.

By using the relations shown below, the fixed frame of reference can be transformed into a wave frame [40,41]:

$$\overline{x} = \overline{X} - ct, \overline{y} = \overline{Y}, \overline{p}(x,y) = \overline{P}(\overline{X,Y},t), \overline{u}(x,y) = \overline{U}(\overline{X,Y},t) - c, \overline{v}(x,y) = \overline{V}(\overline{X,Y},t). \tag{28}$$

So, Eqs. (9)–(12) become

$$\frac{\partial \overline{u}}{\partial \overline{x}} + \frac{\partial \overline{v}}{\partial \overline{y}} = 0, \tag{29}$$

$$\rho_{thnf}\left(\overline{u}\frac{\partial \overline{u}}{\partial \overline{x}} + \overline{v}\frac{\partial \overline{u}}{\partial \overline{y}}\right) = -\frac{\partial \overline{p}}{\partial \overline{x}} + \frac{\partial \overline{S}_{xx}}{\partial \overline{x}} + \frac{\partial \overline{S}_{xy}}{\partial \overline{y}} - \sigma_{thnf} B_0{}^2(\overline{u}+c) + \rho_e E_x + g(\rho\beta_t)_{thnf}(\overline{T} - \overline{T}_0) - \mu_{thnf}\frac{(\overline{u}+c)}{k^*}, \tag{30}$$

$$\rho_{thnf}\left(\overline{u}\frac{\partial \overline{v}}{\partial \overline{x}} + \overline{v}\frac{\partial \overline{v}}{\partial \overline{y}}\right) = -\frac{\partial \overline{p}}{\partial \overline{y}} + \frac{\partial \overline{S}_{xy}}{\partial \overline{x}} + \frac{\partial \overline{S}_{yy}}{\partial \overline{y}}, \tag{31}$$

$$(\rho C_P)_{thnf}\left(\overline{u}\frac{\partial \overline{T}}{\partial \overline{x}} + \overline{v}\frac{\partial \overline{T}}{\partial \overline{y}}\right) = k_{thnf}\left(\frac{\partial^2 \overline{T}}{\partial \overline{x}^2} + \frac{\partial^2 \overline{T}}{\partial \overline{y}^2}\right) + \overline{S}_{xx}\frac{\partial \overline{u}}{\partial \overline{x}} + \overline{S}_{xy}\left(\frac{\partial \overline{u}}{\partial \overline{y}} + \frac{\partial \overline{v}}{\partial \overline{x}}\right) + \overline{S}_{yy}\frac{\partial \overline{v}}{\partial \overline{y}} - \left(\frac{\partial \overline{q}_r}{\partial \overline{x}} + \frac{\partial \overline{q}_r}{\partial \overline{y}}\right) + \sigma_{thnf}\left(E_X{}^2 + B_0{}^2(\overline{u}+c)^2\right). \tag{32}$$

To standardize the governing equations, one can make use of the relations provided below, which are utilized following the process of normalization:

$$x = \frac{\overline{x}}{\lambda}, y = \frac{\overline{y}}{a}, t = \frac{c\overline{t}}{a}, \beta = \frac{a}{\lambda}, u = \frac{\overline{u}}{c}, v = \frac{\overline{v}}{\beta c}, p = \frac{\overline{p}a^2}{\mu_f c\lambda}, \theta = \frac{\overline{T} - T_0}{T_1 - T_0}, S = \frac{\overline{s}a}{\mu_f c}, \varphi = \frac{\overline{\varphi}}{\zeta}, H = \frac{\overline{H}}{a}, Re = \frac{\rho_f ac}{\mu_f}, k = \frac{k^*}{a^2}. \tag{33}$$

The Reynolds number Re and the factor β in Eq. (33) need to be minimal for the Stokes-flow problem to be properly addressed. Under these conditions, equation (9) through (12) that regulate the system can be written as follows:

$$\frac{\partial u}{\partial x} + \frac{\partial v}{\partial y} = 0, \tag{34}$$

$$\left(\frac{\rho_{thnf}}{\rho_f}\right) Re\, \beta \left(u\frac{\partial u}{\partial x}+v\frac{\partial u}{\partial y}\right) = -\frac{\partial p}{\partial x}+\beta\frac{\partial S_{xx}}{\partial x}+\frac{\partial S_{xy}}{\partial y}-\frac{\sigma_{thnf}}{\sigma_f}Ha^2(u+1)+g_r\theta\frac{(\rho\beta_t)_{thnf}}{(\rho\beta_t)_f}+U_{HS}\left(\beta^2\frac{\partial^2\varphi}{\partial x^2}+\frac{\partial^2\varphi}{\partial y^2}\right)-\frac{\mu_{thnf}}{\mu_f}\left(\frac{u+1}{k}\right), \tag{35}$$

$$\left(\frac{\rho_{thnf}}{\rho_f}\right) Re\, \beta^3 \left(u\frac{\partial v}{\partial x}+v\frac{\partial v}{\partial y}\right) = -\frac{\partial p}{\partial y}+\beta^2\frac{\partial S_{xy}}{\partial x}+\beta\frac{\partial S_{yy}}{\partial y}, \tag{36}$$

$$\begin{aligned}\frac{(\rho C_P)_{thnf}}{(\rho C_P)_f} Re\,\Pr\,\beta\left(u\frac{\partial\theta}{\partial x}+v\frac{\partial\theta}{\partial y}\right) = {} & \frac{k_{thnf}}{k_f}\left(\beta^2\frac{\partial^2\theta}{\partial x^2}+\frac{\partial^2\theta}{\partial y^2}\right)+R_n\Pr\left(\beta\frac{\partial}{\partial x}\left(\frac{\partial\theta}{\partial y}\right)+\frac{\partial^2\theta}{\partial y^2}\right)+\Pr Ec\left(\beta S_{xx}\frac{\partial u}{\partial x}+S_{xy}\left(\frac{\partial u}{\partial y}+\beta^2\frac{\partial v}{\partial x}\right)+\beta S_{yy}\frac{\partial v}{\partial y}\right)\\ & +\frac{\sigma_{thnf}}{\sigma_f}\left(S_P+Ha^2PrEc(u+1)^2\right),\end{aligned} \tag{37}$$

where

$$S_{xx}=2\beta\frac{\mu_{thnf}}{\mu_f}\left[1+(n-1)We^2\left(\beta^2\left(\left(\frac{\partial u}{\partial x}\right)^2+\left(\frac{\partial v}{\partial y}\right)^2\right)+\frac{1}{2}\left(\frac{\partial u}{\partial y}+\beta^2\frac{\partial v}{\partial x}\right)^2\right)\right]\frac{\partial u}{\partial x}, \tag{38}$$

$$S_{xy}=\frac{\mu_{thnf}}{\mu_f}\left(\frac{\partial u}{\partial y}+\beta^2\frac{\partial v}{\partial x}\right)\left[1+(n-1)We^2\left(\beta^2\left(\left(\frac{\partial u}{\partial x}\right)^2+\left(\frac{\partial v}{\partial y}\right)^2\right)+\frac{1}{2}\left(\frac{\partial u}{\partial y}+\beta^2\frac{\partial v}{\partial x}\right)^2\right)\right], \tag{39}$$

$$S_{yy}=2\beta\frac{\mu_{thnf}}{\mu_f}\left[1+(n-1)We^2\left(\beta^2\left(\left(\frac{\partial u}{\partial x}\right)^2+\left(\frac{\partial v}{\partial y}\right)^2\right)+\frac{1}{2}\left(\frac{\partial u}{\partial y}+\beta^2\frac{\partial v}{\partial x}\right)^2\right)\right]\frac{\partial v}{\partial y}. \tag{40}$$

In terms of the tangential and orthogonal velocity parts, the stream function (ψ) is introduced as below:

$$u=\frac{\partial\psi}{\partial y}, v=-\frac{\partial\psi}{\partial x}. \tag{41}$$

The non-dimensional governing equations (Eqs. (34)–(37)) can be simplified by utilizing Eqs. (38–40 and 41), along with the assumptions of an infinite wavelength ($\beta\ll 1$) and an inertia-free stream ($Re\approx 0$).

$$\frac{\partial p}{\partial x}=\frac{\mu_{thnf}}{\mu_f}\left[\frac{\partial^3\psi}{\partial y^3}+\frac{n-1}{2}We^2\frac{\partial}{\partial y}\left(\frac{\partial^2\psi}{\partial y^2}\right)^3\right]-\frac{\sigma_{thnf}}{\sigma_f}Ha^2\left(\frac{\partial\psi}{\partial y}+1\right)+U_{HS}\frac{\partial^{2\varphi}}{\partial y^2}+\frac{(\rho\beta_t)_{thnf}}{(\rho\beta_t)_f}g_r\theta-\frac{\mu_{thnf}}{\mu_f k}\left(\frac{\partial\psi}{\partial y}+1\right), \tag{42}$$

$$\frac{\partial p}{\partial y}=0, \tag{43}$$

$$\left(\frac{k_{thnf}}{k_f}+R_n\,Pr\right)\frac{\partial^2\theta}{\partial y^2}+\Pr Ec\frac{\mu_{thnf}}{\mu_f}\left[\left(\frac{\partial^2\psi}{\partial y^2}\right)^2+\frac{n-1}{2}We^2\left(\frac{\partial^2\psi}{\partial y^2}\right)^4\right]+\frac{\sigma_{thnf}}{\sigma_f}\left(S_P+Ha^2PrEc\left(\frac{\partial\Psi}{\partial y}+1\right)^2\right)=0, \tag{44}$$

$$\frac{\partial^2\varphi}{\partial y^2}=K^2\varphi, \tag{45}$$

Differentiation of Equations (42) and (43) with respect to y and x, respectively results in

$$\frac{\mu_{thnf}}{\mu_f}\left(\frac{\partial^4\psi}{\partial y^4}+\frac{n-1}{2}We^2\frac{\partial^2}{\partial y^2}\left(\frac{\partial^2\psi}{\partial y^2}\right)^3\right)-\frac{\sigma_{thnf}}{\sigma_f}Ha^2\frac{\partial^2\psi}{\partial y^2}+U_{HS}\frac{\partial^3\varphi}{\partial y^3}+\frac{g_r(\rho\beta_t)_{thnf}}{(\rho\beta_t)_f}\frac{\partial\theta}{\partial y}-\frac{\mu_{thnf}}{\mu_f k}\frac{\partial^2\psi}{\partial y^2}=0. \tag{46}$$

The followings are chosen as the relevant dimensionless boundary conditions:

$$\psi=0,\frac{\partial^2\psi}{\partial y^2}=0,\frac{\partial\theta}{\partial y}=0,\frac{\partial\varphi}{\partial y}=0, at\ y=0, \psi=F,\frac{\partial\psi}{\partial y}=-1-\frac{2\pi\alpha\varepsilon\beta\cos(2\pi x)}{1-2\pi\alpha\varepsilon\beta\cos(2\pi x)},\theta=1,\varphi=1, at\ y=\mathrm{H}, \tag{47}$$

The mathematical expressions of some parameters generated above can be found below:

$$\begin{aligned}&Ha^2=(\mathrm{B}_0 a)^2\frac{\sigma_f}{\mu_f}, We=\Gamma \mathrm{ca}^{-1}, \Pr=\frac{k_f^{-1}}{(\mu_f C_P)^{-1}}, Ec=\frac{(C_P\Delta T)^{-1}}{c^{-2}}, U_{HS}=\frac{(c\mu_f)^{-1}}{(E_X\varepsilon\varepsilon_0\zeta)^{-1}}, g_r=\left(\frac{c\mu_f}{g(\rho\beta_t)_f\Delta Ta^2}\right)^{-1}, R_n=\left(\frac{3\mu_f C_P K^*}{16\sigma^*(\Delta T)^3}\right)^{-1},\\ &S_P=\frac{\sigma_f {E_X}^2 a^2}{\Delta T k_f}, K=aze\left(\frac{2n_0}{k_b T_{ave}\varepsilon\varepsilon_0}\right)^{\frac{1}{2}}.\end{aligned} \tag{48}$$

The equation below represents the correlation between the dimensionless average flow rates in the static (Q) and traveling (F) reference frames

$$Q = 1 + \int_0^H \left(\frac{\partial \psi}{\partial y}\right) dy. \tag{49}$$

3. Entropy analysis

The second law of thermodynamics suggests that entropy generation within the electro-osmotic pump is influenced by various factors such as radiation and convection heat transfer, fluid resistance, magnetic field friction and function of electric potential. Therefore, the volumetric entropy can be expressed using the below equation, as per theory ([48,49,51]):

$$S_{gen}^{'''} = \frac{1}{T_0{}^2}\left[k_{thnf}(\nabla \overline{T})^2 + \frac{16\sigma^*(T_1 - T_0)^3}{3K^*}(\nabla \overline{T})^2\right] + \frac{1}{T_0}[S.\nabla V] + \frac{\sigma_{thnf}}{T_0}\left[B_0^2 U^2 + E_X^2\right], \tag{50}$$

The dimensionless form of the above relation is expressed here

$$N_S = \left(\frac{k_{thnf}}{k_f} + RnPr\right)\left(\frac{\partial \theta}{\partial y}\right)^2 + \frac{PrEc}{\tau}\frac{\mu_{thnf}}{\mu_f}\left[\frac{\partial^2 \psi}{\partial y^2} + \frac{n-1}{2}We^2\left(\frac{\partial^2 \psi}{\partial y^2}\right)^3\right] + \frac{\sigma_{thnf}}{\sigma_f}\left(\frac{1}{\tau}\right)\left[Ha^2 PrEc\left(\frac{\partial \psi}{\partial y} + 1\right)^2 + S_P\right], \tag{51}$$

The Bejan number for this particular entropy number can be calculated using the following formula:

$$Be = \frac{\left(\frac{k_{thnf}}{k_f} + RnPr\right)\left(\frac{\partial \theta}{\partial y}\right)^2}{\left(\frac{k_{thnf}}{k_f} + RnPr\right)\left(\frac{\partial \theta}{\partial y}\right)^2 + \frac{PrEc}{\tau}\frac{\mu_{thnf}}{\mu_f}\left[\frac{\partial^2 \psi}{\partial y^2} + \frac{n-1}{2}We^2\left(\frac{\partial^2 \psi}{\partial y^2}\right)^3\right] + \frac{\sigma_{thnf}}{\sigma_f}\left(\frac{1}{\tau}\right)\left[Ha^2 PrEc\left(\frac{\partial \psi}{\partial y} + 1\right)^2 + S_P\right]}. \tag{52}$$

From Eq. (45) along with boundary limits define din Eq. (47) can be found as

$$\Phi = exp\langle (H - y)K\rangle\ (1 + exp\ 2\ Ky) \big/ \left(1 + e^{2KH}\right), \tag{53}$$

4. Numerical results and comparison with the existing literature

With the help of the Mathematica numerical program "NDSolve," we employ a shooting strategy to numerically solve the coupled differential equations Eqs. (44) and (46). The study presented here is compared to that presented in Ref. [15]; see Table 2 for details. This data also hints that, compared to Williamson fluid, Carreau fluid has better heat transfer in the presence of porous material [15]. The final column of the table shows that the rate of thermal exchange increases by almost 11–20% when using Carreau fluid as compared to the Williamson model in Ref. [15], indicating that Carreau fluid is superior to Williamson fluid in terms of increasing heat transfer in the flow. The results of g_r, R_n, and U_{HS} are suggested in Table 3. The table shows that while large values of g_r and R_n cause a decrease in velocity, larger values of U_{HS} cause an increase. To provide a rough visual comparison between the current work and the prior study [15], Fig. 2 is given. Taking the limiting situation of $We = 0, n = 3$, it is clear that the present study is a recalculation of the

Table 2
Comparison of current heat transfer rate with previous study [15].

Ha	Data of [15]	Current work with limiting cases $\boldsymbol{We = 0,\ n = 3,\ k^{'} \to \infty}$	Difference between readings	Current work with $\boldsymbol{We = 0.5}$, $\boldsymbol{n = 2, k^{'} = 0.05}$	% increase in heat transfer rate of Carreau fluid with Williamson fluid [15]
0.5	1.19513	1.24646	0.05130	1.43763	20.29%
1	1.32504	1.3663 0	0.04126	1.56392	18.03%
1.5	1.54145	1.56523	0.02378	1.77515	15.16%
2	1.83713	1.84235	0.00522	2.07245	12.81%
2.5	2.20715	2.19674	−0.01041	2.45738	11.34%

Table 3
Effects of various physical factors on the velocity profile.

y	Velocity profile for $\boldsymbol{g_r}$		Velocity profile for $\boldsymbol{R_n}$		Velocity profile for $\boldsymbol{U_{HS}}$	
	$g_r = 0.5$	$g_r = 0.6$	$R_n = 1$	$R_n = 1.5$	$U_{HS} = -2.5$	$U_{HS} = 2.5$
0.0	1.438	1.437	1.438	1.391	1.438	1.439
0.1	1.436	1.436	1.436	1.389	1.436	1.437
0.2	1.433	1.432	1.433	1.386	1.433	1.434
0.3	1.427	1.426	1.427	1.381	1.427	1.428
0.4	1.419	1.418	1.419	1.374	1.419	1.420
0.5	1.408	1.407	1.408	1.364	1.408	1.409
0.6	1.395	1.394	1.395	1.352	1.395	1.396
0.7	1.379	1.378	1.379	1.338	1.379	1.380
0.8	1.359	1.358	1.359	1.321	1.359	1.360
0.9	1.334	1.333	1.334	1.298	1.334	1.335
1.0	1.296	1.294	1.296	1.263	1.296	1.297

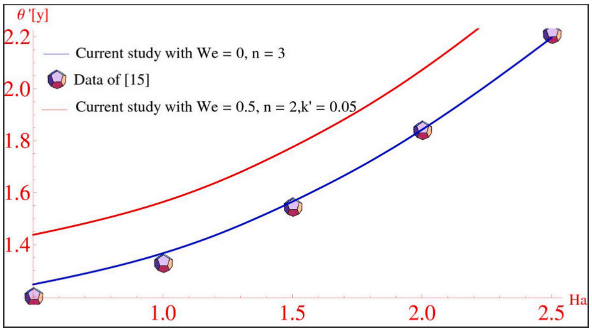

Fig. 2. Comparison and validity of the current work with existing literature.

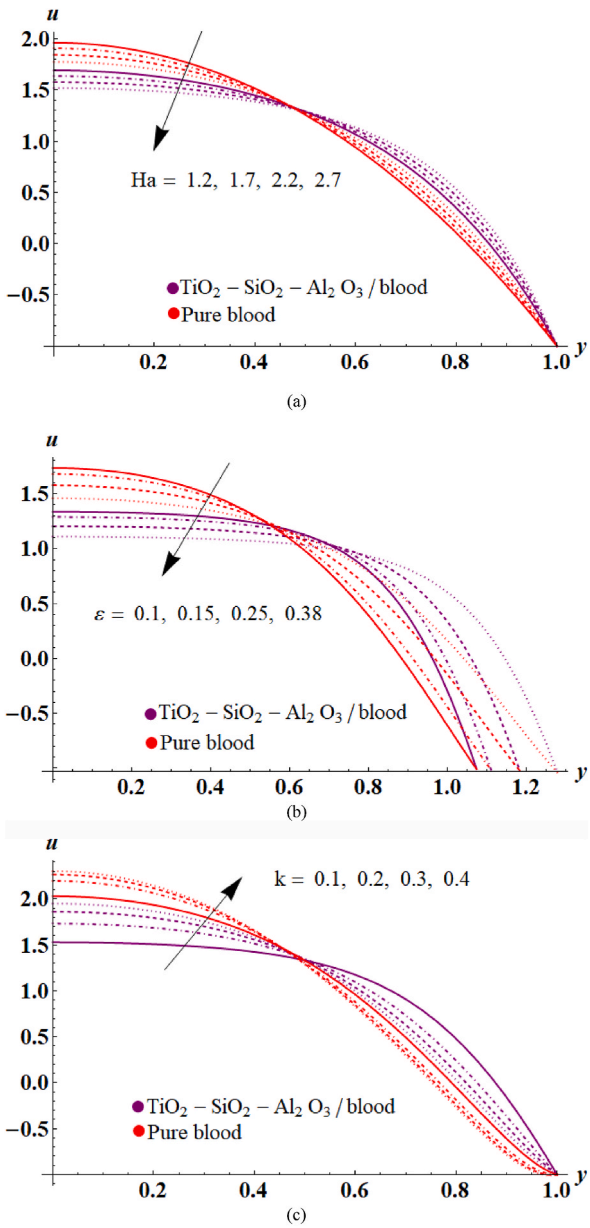

Fig. 3. (a,b,c): Variation in the velocity function due to (a) *Ha* (b) ε (c) *k*. The other parameters are $We = 0.1, n = 2, Ec = 0.01, Pr = 0.9, x = 0.12, g_r = 0.5, R_n = 2, U_{HS} = -2.5, K = 5, S_P = 0.5$..

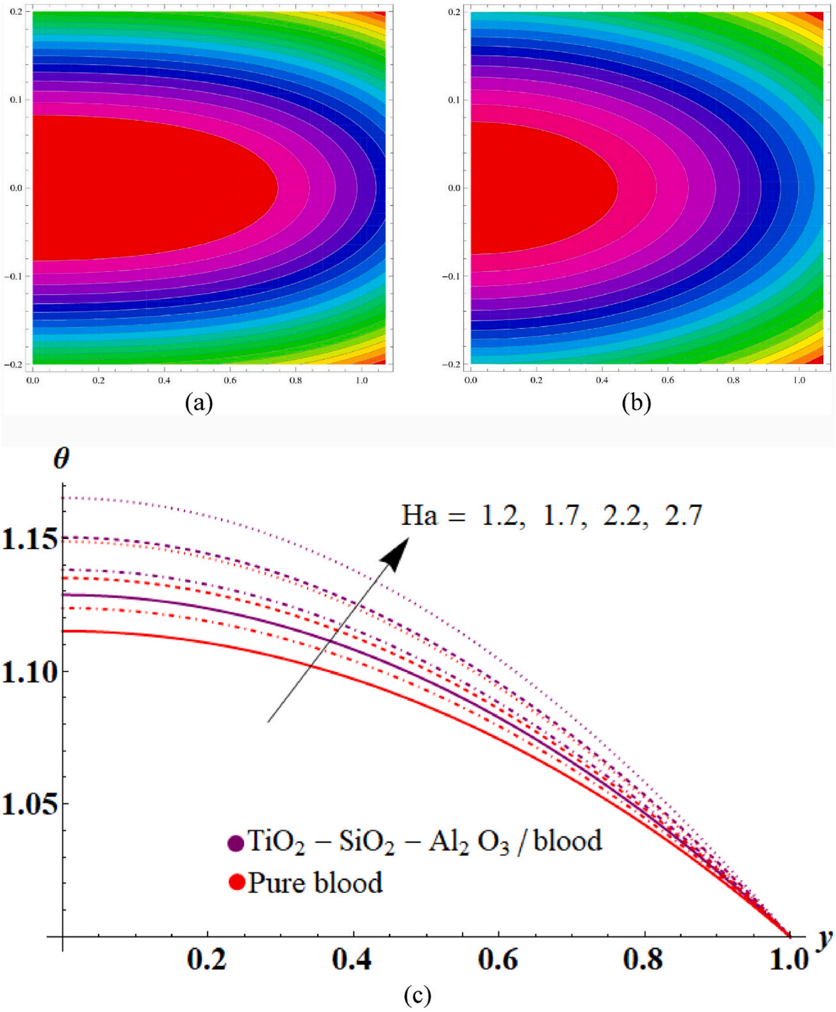

Fig. 4. (a,b,c): Variation in the temperature profile for Ha. The other parameters are $We = 0.1, n = 2, Ec = 0.1, Pr = 1, x = 0.12, g_r = 0.5, R_n = 1, U_{HS} = -2.5, K = 7, S_P = 0.5$..

results from the work [15] about the heat transfer rate profile. Furthermore, this research demonstrates that the Hartman number accounts for the increase in heat exchange rate that occurs during the flow.

Moreover, In this part, we will talk in detail about how the numerical solutions can be measured in different ways for the velocity component (u), heat transfer function (θ), entropy optimization function (N_S), the Bejan number Be and the stream function (ψ). Different graphs are constructed and shown in Figs. 3–10.

Fig. 3(a) shows that, the relationship between velocity and Hartmann number is not constant; rather, it changes over a wide range of values for this quantity. In magnetohydrodynamic (MHD) systems, the ratio of the Lorentz force to the viscous force is defined by a parameter known as the Hartmann number. It is commonly used to study the effects of magnetic fields on fluids that conduct electricity. Fig. 3(a) depicts flow in a magnetic field, where the fluid's velocity is altered according to the Hartmann number. The graph indicates that the velocity drops for Hartmann numbers between 0 and 0.5. This indicates that the fluid's permeability decreases with increasing magnetic field strength. One theory proposes that this is because the fluid's velocity is dampened by a Lorentz force generated by the magnetic field. The fluid velocity consequently reduces with increasing magnetic field strength. On the other hand, the figure also shows that the velocity rises with an increase in the Hartmann number in the range [0.5, 1]. This means that there is a region of Hartmann numbers in which the fluid velocity rises as a function of magnetic field strength. The magnetic field could be responsible for instability in the flow that increases the mixing of the fluid and the speed with which it moves. This phenomenon occurs in MHD systems when the magnetic field induces a turbulent flow pattern that improves mixing and transport. In this context, it is also noted that the flow and velocity of a fluid may exhibit varying behaviors depending on the fluid type under investigation. The blood's base fluid behavior is compared to that of a ternary-hybrid nanofluid in this scenario. The message is clear: the simple blood flows more quickly and readily through the conduit than the nanofluid. Fig. 3(b) plots the velocity profile versus cilia length ε and shows how it varies over time. The velocity profile shifts noticeably as a function of the cilia length variation, as shown by the graph. When ε is increased, the left side of the channel experiences a decrease in flow velocity while the right-side experiences an increase. The

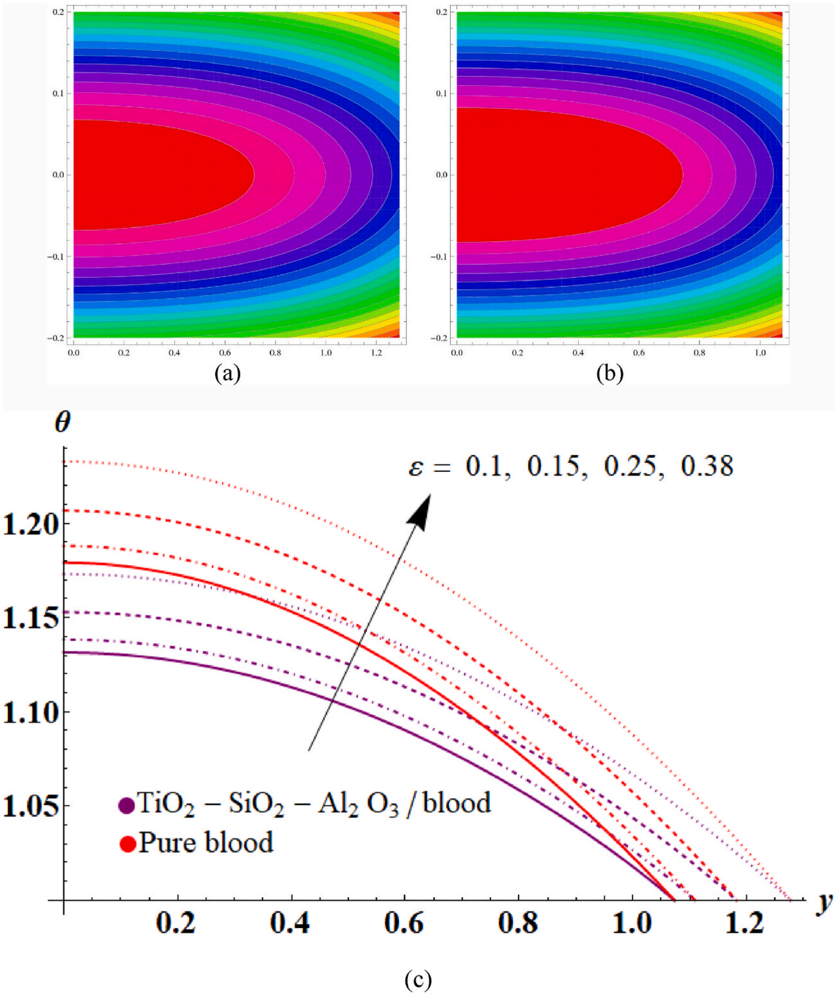

Fig. 5. (a,b,c): Variation in the temperature profile for Ha. The other parameters are $We = 0.1, n = 2, Ec = 0.1, Pr = 1, x = 0.12, g_r = 0.5, R_n = 1, U_{HS} = -2.5, K = 7, S_P = 0.5$..

following is a physical explanation for this phenomenon. The beating action of the cilia structures aids in the transport of fluids over the surface. The length of these structures is represented here by the cilia length parameter. The beating motion of the cilia is less efficient at transporting fluids close to the left channel domain as cilia length raises. As a result, fluid velocity is reduced there. However, the longer cilia are able to generate a stronger beating motion in the right directed region, resulting in a greater flow speed there. Therefore, the considerable effect of cilia length factor on fluid velocity distribution in the channel is illustrated by the graph in Fig. 3(b). This knowledge can be applied to the development of improved cilia-based microfluidic devices. The effects of the porosity factor k' are estimated in Fig. 3(c). The left side of the domain shows an increased velocity profile due to a porous material, while the right side shows the opposite. The physical explanation for this is that, as a fluid goes through a porous medium, it will face barriers, forcing it to alter its trajectory so that it may flow around them. In some cases, the fluid's flow can be concentrated by this deflection, leading to higher localized velocities.

Temperature contours illustrating the impact of the Hartman number Ha, the cilia length parameter ε, and the porosity parameter k' on the heat transfer profile are generated in Fig. 4(a–c). Heat transfer may be seen to fluctuate directly with the increase of both variables. Fig. 4(a)–(c) depicts the axial variation of the temperature function with the Hartman number Ha. The plot shows that the magnetic field intensity, as measured by the Hartman number, correlates directly with the temperature distribution. The graph illustrates that an increase in magnetic field strength leads to a higher heat transfer rate, as the Hartman number shows a clear association with the temperature profile. Heat transfer rate is increased by the incorporation of ternary hybrid particles into the base fluid, suggesting that this type of nanofluid is responsible for the increased thermal exchange intensity observed in the flow. Heat transfer improves as a function of the cilia length parameter, as shown in Fig. 5(a–c). In contrast to pure blood, the plot shows that the hybrid nanofluid has a decreased heat transfer rate. This may be because heat transmission efficiency is diminished by the hybrid nanofluid's increased complexity. These findings, taken as a whole, demonstrate the value of magnetic fields and particle additions in speeding up the rate at which heat is transferred through a fluid. However, the complexity of the fluid system must be taken into account before any

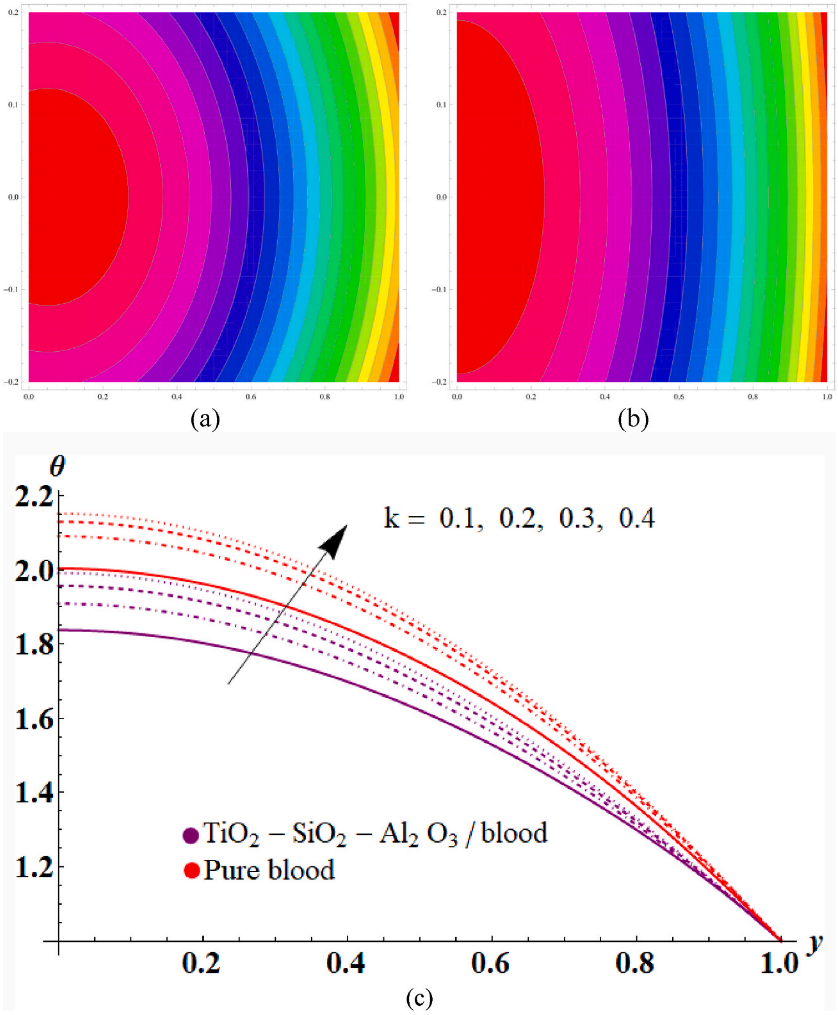

Fig. 6. (a,b,c): Variation in the temperature for k. The other parameters are $We = 0.1, n = 2, Ec = 0.1, Pr = 1, x = 0.12, g_r = 0.5, R_n = 1, U_{HS} = -2.5, K = 7, S_P = 0.5$..

additives are introduced to guarantee that the system's thermal behavior is not adversely affected. From Fig. 6(a–c), we may deduce that the medium's porosity, denoted by the symbol k', is intended to raise the flow temperature. Porous media often have a larger surface area than nonporous media. This increases the potential for heat transfer between the fluid and the solid matrix of the porous media. That's why it's possible to increase the heat transmission rate.

The effect of an increasing Hartman number on the entropy generation rate Ns is graphically depicted in Fig. 7(a–c). It is easy to see from the diagram that as the applied magnetic field increases, so does the entropy of the flow. For a given magnetic field strength, the Lorentz force induced by it grows in proportion to the Hartmann number. The pace, at which entropy is created, increases as a result of the increased mixing and disturbance of the fluid flow. The entropy rate of hybrid nanofluids is claimed to be greater than that of pure fluids (blood) in 75% of the domain, whereas in the remaining 25%, the reverse trend is observed. Because the nanoparticles make the fluid more viscous and less thermally conductive, they induce greater friction and thermal losses, which in turn generates more entropy. In 75% of the domain, the hybrid nanofluid has a greater entropy rate than the pure fluid (blood), suggesting that its employment may not be optimal there. However, the usage of the hybrid nanofluid may be helpful for lowering entropy formation in the other 25% of the domain where the opposite behavior is documented. The influence of cilia length on the intensity of entropy production is seen in the following entropy graph (Fig. 7(b)), which suggests that the rate of entropy is proportional to the cilia length on the left side of the domain, roughly up to $y = 0.5$ for the base fluid and $y = 0.7$ for the hybrid nanofluid. The contrary is true if we examine the domain $y > 0.5$ and 0.7, where the entropy rate drops off precipitously, suggesting that cilia length can be highly useful in lowering the entropy generation rate. Longer cilia may cause a more ordered flow pattern, decreasing mixing and, in turn, the rate at which entropy is generated. In addition, slower flow velocities may result from longer cilia, which in turn reduces the kinetic energy and, by extension, the rate at which entropy is generated. It is determined that the entropy rate due to a porous medium is accelerating and large on the right-hand domain, as shown in Fig. 7(c), which illustrates the effect of the porosity factor on entropy creation.

The Bejan number profile, shown in Fig. 8(a–c), is a measure of the irreversibility of heat transfer relative to the overall entropy

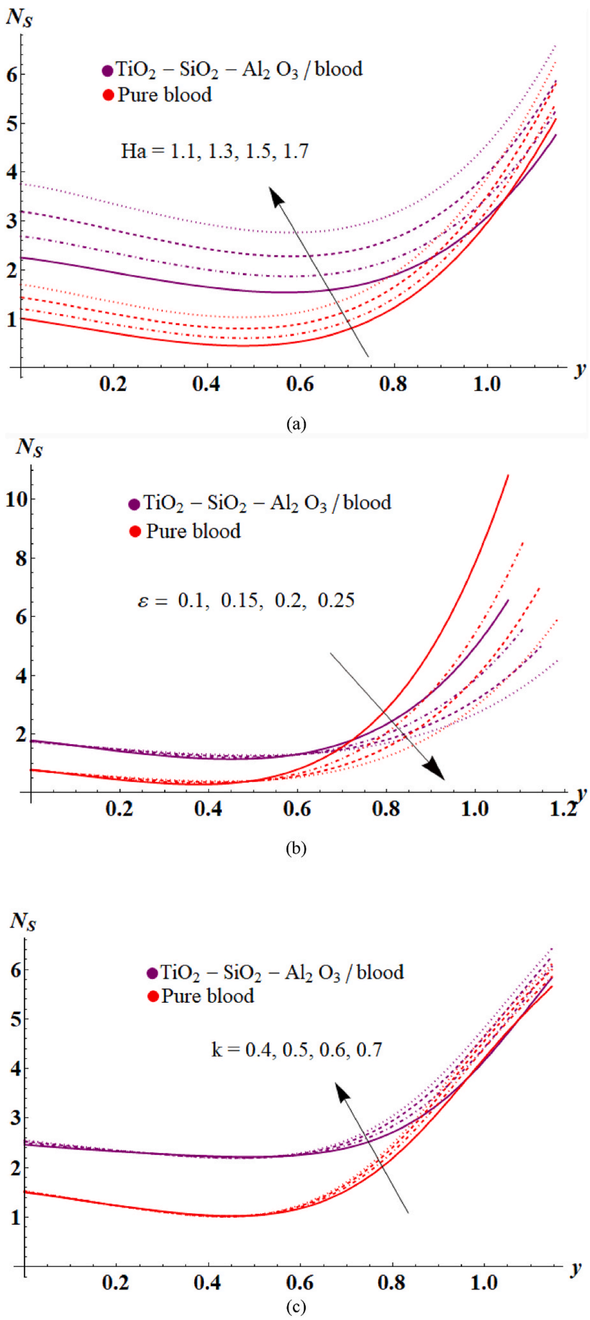

Fig. 7. (a,b,c): Variation in the entropy expression due to (a) Ha (b) ε (c) k. The other parameters are $We = 0.01, n = 2, Ec = 0.1, Pr = 2, x = 0.12, g_r = 0.1, R_n = 0.9, U_{HS} = -3, K = 4, S_P = 1$..

generated in a fluid flow. When describing the intensity of a magnetic field in a conducting fluid, the Hartman number is used. Fig. 8(a) shows that when the magnetic field strength increases, the irreversibility of the heat transfer process increases, and the efficiency of the heat transfer decreases. The plot also reveals that the magnetic field has a greater influence on the flow at the system's boundary, as expected, for bigger values of the axial coordinate y. Interestingly, as the magnetic field intensity increases, the curves for the hybrid nanofluid fall below those for pure blood, indicating that the presence of nanoparticles in the fluid mitigates the effect of the magnetic field on the irreversibility of the heat transfer. Fig. 8(b) shows that as the cilia length grow, the Bejan number profile drops, implying an inverse relationship between the two. A cell's cilia are hair-like structures that can promote fluid mixing and increased heat transmission. However, longer cilia may cause less orderly and more turbulent flow patterns, which may hinder heat transfer. Consequently, the decreased efficiency of heat transfer may account for the smaller Bejan number profile at increasing cilia lengths. When an electric field is given to a liquid, the liquid will move, a phenomenon known as electro-osmotic flow. The interaction between the electric

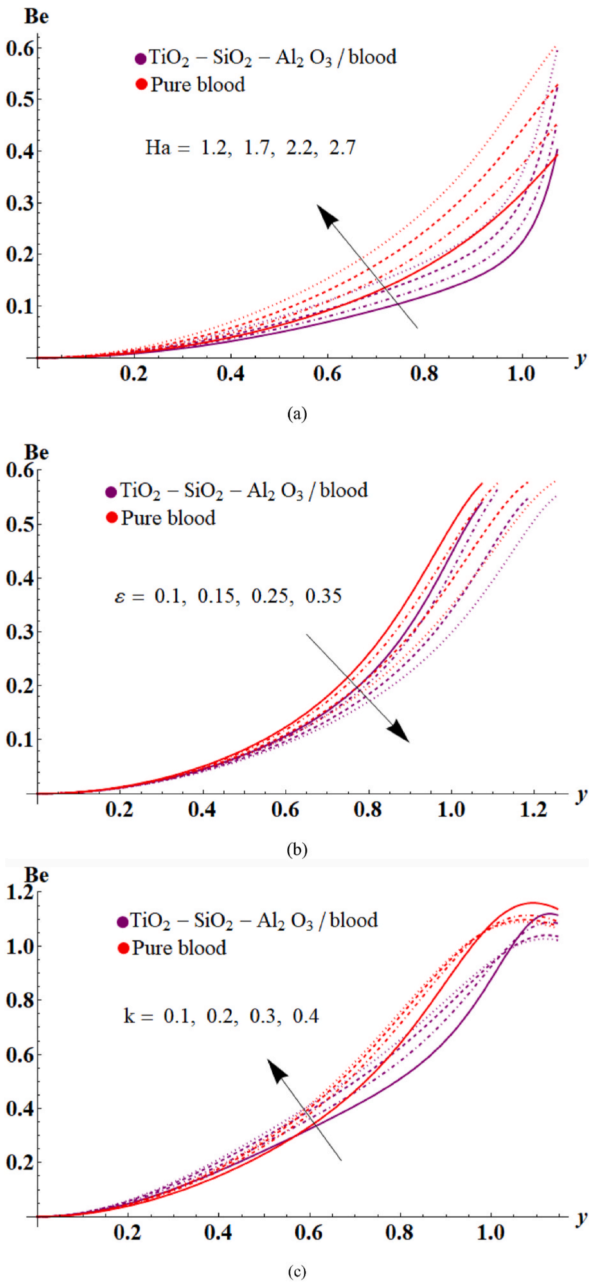

Fig. 8. (a,b,c): Variation in the Bejan number due to (a) Ha (b) ε (c) k. The other parameters are $We = 0.1, n = 2, Ec = 0.1, Pr = 1.5, x = 0.12, g_r = 0.5, R_n = 2.5, U_{HS} = -1, K = 5, S_P = 0.5$..

charges on the channel's surface and the ions present in the liquid causes this phenomenon, which manifests itself in microscopic channels or capillaries. Fig. 8(c) depicts the effect of the porosity parameter k' on the Bejan number profile; as the impact of the porosity parameter increases, the Bejan number curves rise.

The effect of the Hartman number on streamlines is depicted in Fig. 9 (a,b). A larger inner circulating bolus is seen as the Hartman number rises, indicating that a more powerful magnetic field slows flow through its resistive effect on flow speed. The streamlines under cilia length variation are shown in Fig. 10 (a,b). When the ciliary length is increased, the resulting boluses are smaller, suggesting that the larger cilia exert more force on the fluid particles, leading to a higher flow rate.

5. Conclusions

The system of non-linear coupled differential equations and boundary conditions is solved for the mixed convection case by employing a shooting method technique with the help of the built-in numerical program "NDSolve" of the computational software

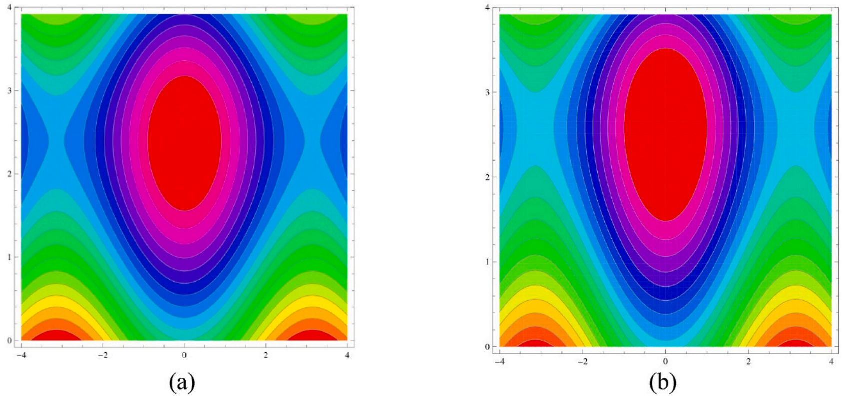

Fig. 9. (a,b): Streamlines for *Ha*.

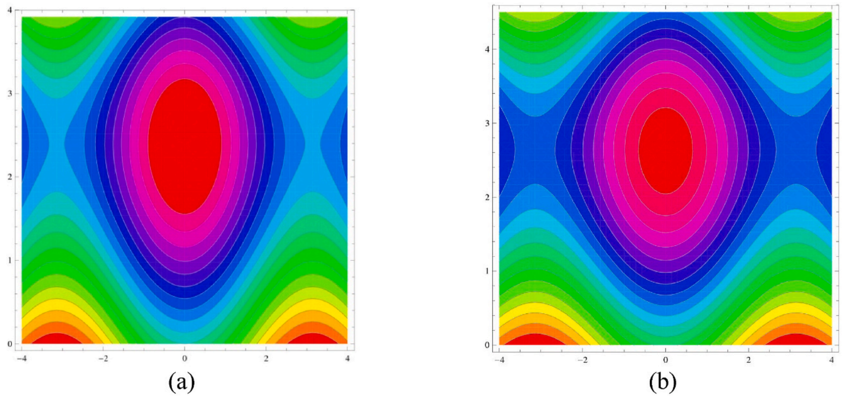

Fig. 10. (a,b): Streamlines for ε.

Mathematica. The solutions for the velocity distribution (u), the stream function, the temperature distribution, the entropy generation number, and the Bejan number are all graphically shown. Titanium oxide, silica, and aluminum oxide all make up 2% of the ternary nanofluid's total solid nanoparticle volume percentage, for a total solid nanoparticle volume percentage of 6% of the base fluid. The following are the most important takeaways from the illustrated discussion:

- Increasing the Hartmann number causes a drop in velocity in the left domain, while increasing it in the right domain.Depending on the fluid type, the flow and velocity characteristics may change.
- The distribution of fluid velocities in the channel is highly sensitive to the cilia length parameter. This knowledge can be applied to the development of improved cilia-based microfluidic devices.
- There is a direct correlation between the Hartman number and the temperature profile, demonstrating that the heat transfer rate is growing with increasing the strength of the magnetic field; the flow velocity remains high with porous medium in the left domain but is low in the right domain. Increasing the intensity of heat exchange in the flow is a result of the incorporation of ternary hybrid particles into the base fluid.
- The heat transmission rate of the hybrid nanofluid is lower than that of pure blood, which may be attributable to the hybrid nanofluid's increased complexity. The flow heats up because of the porosity.
- Ciliary length, however, is intended to mitigate the impacts of irreversibility; this is in contrast to the Hartman number and porosity factor, which generate the system entropy and Bejan number.
- The length of the cilia has an opposing effect on the number and size of trapping boluses when a magnetic field is present.

6. Future directions

- Explore the impact of various operating conditions on ciliary flow and entropy formation with in-depth parametric analyses. This can be done by investigating the effects of a broader range of Hartman numbers, trying out other nanofluid properties, or taking into account alternative geometries and boundary conditions.
- The current mathematical model should be expanded so that it can account for a wider range of physical occurrences. Examples of such research include examining the behavior of ciliary systems in non-Newtonian fluids with complicated rheological properties, including the impacts of fluid-solid interactions, and considering the impact of microscale fluid dynamics.

Authors' statement

It is stated that all the authors contributed equally in various parts of the study.

Declaration of competing interest

The authors declare that they have no known competing financial interests or personal relationships that could have appeared to influence the work reported in this paper.

Data availability

No data was used for the research described in the article.

Acknowledgement

Princess Nourah bint Abdulrahman University Researchers Supporting Project number (PNURSP2023R 371), Princess Nourah bint Abdulrahman University, Riyadh, Saudi Arabia.

References

[1] M.A. Sleigh, The Biology of Cilia and Flagella: International Series of Monographs on Pure and Applied Biology: Zoology, vol. 12, Elsevier, 2016, 12.
[2] J. Blake, A model for the micro-structure in ciliated organisms, J. Fluid Mech. 55 (1) (1972) 1–23.
[3] J. Blake, Flow in tubules due to ciliary activity, Bull. Math. Biol. 35 (1973) 513–523.
[4] T.J. Lardner, W.J. Shack, Cilia transport, Bull. Math. Biophys. 34 (1972) 325–335.
[5] N. Sher Akbar, S. Akhtar, Metachronal wave form analysis on cilia-driven flow of non-Newtonain Phan–Thien–Tanner fluid model: a physiological mathematical model, Proc. IME E J. Process Mech. Eng. (2022), 09544089221140703.
[6] K.S. Mekheimer, A.Z. Zaher, W.M. Hasona, Entropy of AC electro-kinetics for blood mediated gold or copper nanoparticles as a drug agent for thermotherapy of oncology, Chin. J. Phys. 65 (2020) 123–138.
[7] S. Shaw, D. Tripathi, Impact of drug carrier shape, size, porosity and blood rheology on magnetic nanoparticle-based drug delivery in a microvessel, Colloids Surf. A Physicochem. Eng. Asp. 639 (2022), 128370.
[8] S. Munawar, N. Saleem, A.J. Chamkha, A. Mehmood, A.U. Dar, Lubricating hot stretching membrane with a thin hybrid nanofluid squeezed film under oscillatory compression, Eur. Phys. J. Plus 136 (8) (2021) 833.
[9] N. Saleem, S. Munawar, D. Tripathi, Entropy analysis in ciliary transport of radiated hybrid nanofluid in presence of electromagnetohydrodynamics and activation energy, Case Stud. Therm. Eng. 28 (2021), 101665.
[10] M.A.Z. Raja, M. Shoaib, R. Tabassum, M.I. Khan, R.P. Gowda, B.C. Prasannakumara, W.F. Xia, Intelligent computing for the dynamics of entropy optimized nanofluidic system under impacts of MHD along thick surface, Int. J. Mod. Phys. B 35 (26) (2021), 2150269.
[11] S.U. Choi, J.A. Eastman, *Enhancing thermal Conductivity of Fluids with nanoparticles*(No. ANL/MSD/CP-84938; CONF-951135-29), Argonne National Lab.(ANL), Argonne, IL (United States), 1995.
[12] W. Ahmed, S.N. Kazi, Z.Z. Chowdhury, M.R.B. Johan, S. Mehmood, M.E.M. Soudagar, M.S. Ahmad, Heat transfer growth of sonochemically synthesized novel mixed metal oxide ZnO+ Al2O3+ TiO2/DW based ternary hybrid nanofluids in a square flow conduit, Renew. Sustain. Energy Rev. 145 (2021), 111025.
[13] Z. Xuan, Y. Zhai, M. Ma, Y. Li, H. Wang, Thermo-economic performance and sensitivity analysis of ternary hybrid nanofluids, J. Mol. Liq. 323 (2021), 114889.
[14] T. Elnaqeeb, I.L. Animasaun, N.A. Shah, Ternary-hybrid nanofluids: significance of suction and dual-stretching on three-dimensional flow of water conveying nanoparticles with various shapes and densities, Z. Naturforsch. 76 (3) (2021) 231–243.
[15] S. Munawar, N. Saleem, Mixed convective cilia triggered stream of magneto ternary nanofluid through elastic electroosmotic pump: a comparative entropic analysis, J. Mol. Liq. 352 (2022), 118662.
[16] S. Manjunatha, V. Puneeth, B.J. Gireesha, A. Chamkha, Theoretical study of convective heat transfer in ternary nanofluid flowing past a stretching sheet, J. Appl. Comput. Mech. 8 (4) (2022) 1279–1286.
[17] B. Ali, S.A. Khan, A.K. Hussein, T. Thumma, S. Hussain, Hybrid nanofluids: significance of gravity modulation, heat source/sink, and magnetohydrodynamic on dynamics of micropolar fluid over an inclined surface via finite element simulation, Appl. Math. Comput. 419 (2022), 126878.
[18] S.A. Khan, C. Eze, K.T. Lau, B. Ali, S. Ahmad, S. Ni, J. Zhao, Study on the novel suppression of heat transfer deterioration of supercritical water flowing in vertical tube through the suspension of alumina nanoparticles, Int. Commun. Heat Mass Tran. 132 (2022), 105893.
[19] S.A. Khan, B. Ali, C. Eze, K.T. Lau, L. Ali, J. Chen, J. Zhao, Magnetic dipole and thermal radiation impacts on stagnation point flow of micropolar based nanofluids over a vertically stretching sheet: finite element approach, Processes 9 (7) (2021) 1089.
[20] B. Ali, S. Hussain, Y. Nie, S.A. Khan, S.I.R. Naqvi, Finite element simulation of bioconvection Falkner–Skan flow of a Maxwell nanofluid fluid along with activation energy over a wedge, Phys. Scripta 95 (9) (2020), 095214.
[21] D. Burgreen, F.R. Nakache, Electrokinetic flow in ultrafine capillary slits1, J. Phys. Chem. 68 (5) (1964) 1084–1091.
[22] R.E. Abo-Elkhair, K.S. Mekheimer, A.M.A. Moawad, Combine impacts of electrokinetic variable viscosity and partial slip on peristaltic MHD flow through a micro-channel, Iran. J. Sci. Technol. Trans. A-Science 43 (2019) 201–212.
[23] M.K. Chaube, A. Yadav, D. Tripathi, O.A. Bég, Electroosmotic flow of biorheological micropolar fluids through microfluidic channels, Korea Aust. Rheol. J. 30 (2018) 89–98.
[24] K. Ramesh, D. Tripathi, M.M. Bhatti, C.M. Khalique, Electro-osmotic flow of hydromagnetic dusty viscoelastic fluids in a microchannel propagated by peristalsis, J. Mol. Liq. 314 (2020), 113568.
[25] P. Jayavel, R. Jhorar, D. Tripathi, M.N. Azese, Electroosmotic flow of pseudoplastic nanoliquids via peristaltic pumping, J. Braz. Soc. Mech. Sci. Eng. 41 (2019) 1–18.
[26] H. Xu, I. Pop, Q. Sun, Fluid flow driven along microchannel by its upper stretching wall with electrokinetic effects, Appl. Math. Mech. 39 (2018) 395–408.
[27] D. Tripathi, A. Yadav, O.A. Bég, R. Kumar, Study of microvascular non-Newtonian blood flow modulated by electroosmosis, Microvasc. Res. 117 (2018) 28–36.
[28] J. Akram, N.S. Akbar, E.N. Maraj, A comparative study on the role of nanoparticle dispersion in electroosmosis regulated peristaltic flow of water, Alex. Eng. J. 59 (2) (2020) 943–956.
[29] S.L. Sun, D. Liu, Y.Z. Wang, Y.L. Qi, H.B. Kim, Convective heat transfer and entropy generation evaluation in the Taylor–Couette flow under the magnetic field, Int. J. Mech. Sci. 252 (2023), 108373.
[30] A. Mahdy, F.M. Hady, R.A. Mohamed, O.A. Abo-zaid, Activation energy effectiveness in dusty Carreau fluid flow along a stretched cylinder due to nonuniform thermal conductivity property and temperature-dependent heat source/sink, Heat Trans. 50 (6) (2021) 5760–5778.
[31] Z. Alloui, P. Vasseur, Natural convection of Carreau–Yasuda non-Newtonian fluids in a vertical cavity heated from the sides, Int. J. Heat Mass Tran. 84 (2015) 912–924.
[32] C.S.K. Raju, M.M. Hoque, N.N. Anika, S.U. Mamatha, P. Sharma, Natural convective heat transfer analysis of MHD unsteady Carreau nanofluid over a cone packed with alloy nanoparticles, Powder Technol. 317 (2017) 408–416.

[33] Y.J. Lim, S. Shafie, S.M. Isa, N.A. Rawi, A.Q. Mohamad, Impact of chemical reaction, thermal radiation and porosity on free convection Carreau fluid flow towards a stretching cylinder, Alex. Eng. J. 61 (6) (2022) 4701–4717.
[34] V.K. Sud, G.S. Sekhon, R.K. Mishra, Pumping action on blood by a magnetic field, Bull. Math. Biol. 39 (3) (1977) 385–390.
[35] K. Maqbool, S. Shaheen, A.B. Mann, Exact solution of cilia induced flow of a Jeffrey fluid in an inclined tube, SpringerPlus 5 (1) (2016) 1–16.
[36] T. Hayat, N. Saleem, S. Mesloub, N. Ali, Magnetohydrodynamic flow of a Carreau fluid in a channel with DifferentWave forms, Z. Naturforsch. 66 (3–4) (2011) 215–222.
[37] K. Ramesh, D. Tripathi, O.A. Bég, Cilia-assisted hydromagnetic pumping of biorheological couple stress fluids, Propul. Power Res. 8 (3) (2019) 221–233.
[38] N. Saleem, S. Akram, F. Afzal, E.H. Aly, A. Hussain, Impact of velocity second slip and inclined magnetic field on peristaltic flow coating with Jeffrey fluid in tapered channel, Coatings 10 (1) (2020) 30.
[39] L. Shi, Y. Hu, Y. He, Magnetocontrollable convective heat transfer of nanofluid through a straight tube, Appl. Therm. Eng. 162 (2019), 114220.
[40] A. Riaz, H. Alolaiyan, A. Razaq, Convective heat transfer and magnetohydrodynamics across a peristaltic channel coated with nonlinear nanofluid, Coatings 9 (12) (2019) 816.
[41] S. Akram, E.H. Aly, F. Afzal, S. Nadeem, Effect of the variable viscosity on the peristaltic flow of Newtonian fluid coated with magnetic field: application of adomian decomposition method for endoscope, Coatings 9 (8) (2019) 524.
[42] Y. Kazemian, S. Rashidi, J.A. Esfahani, N. Karimi, Simulation of conjugate radiation–forced convection heat transfer in a porous medium using the lattice Boltzmann method, Meccanica 54 (2019) 505–524.
[43] M. Mesgarpour, R. Habib, M.S. Shadloo, N. Karimi, A combination of large eddy simulation and physics-informed machine learning to predict pore-scale flow behaviours in fibrous porous media: a case study of transient flow passing through a surgical mask, Eng. Anal. Bound. Elem. 149 (2023) 52–70.
[44] D.A. Nield, A. Bejan, Convection in Porous Media, vol. 3, springer, New York, 2006.
[45] N.S. Akbar, A.W. Butt, D. Tripathi, O.A. Bég, Physical hydrodynamic propulsion model study on creeping viscous flow through a ciliated porous tube, Pramana 88 (2017) 1–9.
[46] N. Manzoor, K. Maqbool, O.A. Bég, S. Shaheen, Adomian decomposition solution for propulsion of dissipative magnetic Jeffrey biofluid in a ciliated channel containing a porous medium with forced convection heat transfer, Heat Tran. Asian Res. 48 (2) (2019) 556–581.
[47] K. Javid, U.F. Alqsair, M. Hassan, M.M. Bhatti, T. Ahmad, E. Bobescu, Cilia-assisted flow of viscoelastic fluid in a divergent channel under porosity effects, Biomech. Model. Mechanobiol. 20 (2021) 1399–1412.
[48] W. Aich, K. Javid, K. Al-Khaled, K. Gachem, D. Khan, S.U. Khan, L. Kolsi, The ciliated flow of water-based graphene oxide and copper nanoparticles (GO-Cu/H2O) in a complex permeable tube with entropy generation phenomenon, Waves Random Complex Media (2022) 1–17.
[49] R. Ellahi, S.Z. Alamri, A. Basit, A. Majeed, Effects of MHD and slip on heat transfer boundary layer flow over a moving plate based on specific entropy generation, J. Taibah Univ. Sci. 12 (4) (2018) 476–482.
[50] A. Majeed, A. Zeeshan, S.Z. Alamri, R. Ellahi, Heat transfer analysis in ferromagnetic viscoelastic fluid flow over a stretching sheet with suction, Neural Comput. Appl. 30 (6) (2018) 1947–1955.
[51] S. Shaheen, K. Maqbool, R. Ellahi, S.M. Sait, Heat transfer analysis of tangent hyperbolic nanofluid in a ciliated tube with entropy generation, J. Therm. Anal. Calorim. 144 (2021) 2337–2346.
[52] M.M. Bhatti, S.Z. Alamri, R. Ellahi, S.I. Abdelsalam, Intra-uterine particle–fluid motion through a compliant asymmetric tapered channel with heat transfer, J. Therm. Anal. Calorim. 144 (2021) 2259–2267.
[53] M.M. Bhatti, R. Ellahi, Numerical investigation of non-Darcian nanofluid flow across a stretchy elastic medium with velocity and thermal slips, Numer. Heat Tran., Part B: Fundamentals 83 (5) (2023) 323–343.
[54] S. Shaheen, M.B. Arain, K.S. Nisar, A. Albakri, M.D. Shamshuddin, A case study of heat transmission in a Williamson fluid flow through a ciliated porous channel: a semi-numerical approach, Case Stud. Therm. Eng. 41 (2022), 102523 ([Google Scholar]).